Chemical Engineering Journal 468 (2023) 143507

Contents lists available at ScienceDirect

Chemical Engineering Journal

journal homepage: www.elsevier.com/locate/cej

Cation-deficient T-Nb_2O_5/graphene Hybrids synthesized via chemical oxidative etching of MXene for advanced lithium-ion capacitors

Lei Wang [a,b], Xiong Zhang [a,b,*], Chen Li [a], Yanan Xu [a], Yabin An [a,b], Wenjie Liu [a,b], Tao Hu [a,b], Sha Yi [a], Kai Wang [a,b], Xianzhong Sun [a], Yue Gong [c], Zhong-Shuai Wu [d,*], Yanwei Ma [a,b,e,*]

[a] *Institute of Electrical Engineering, Chinese Academy of Sciences, Beijing 100190, China*
[b] *School of Engineering Sciences, University of Chinese Academy of Sciences, Beijing 100049, China*
[c] *CAS Key Laboratory of Standardization and Measurement for Nanotechnology, CAS Center for Excellence in Nanoscience, National Center for Nanoscience and Technology, Beijing 100190, China*
[d] *State Key Laboratory of Catalysis, Dalian Institute of Chemical Physics, Chinese Academy of Sciences, Dalian 116023, China*
[e] *School of Materials Science and Engineering, Zhengzhou University, Zhengzhou, Henan 450001, China*

ARTICLE INFO

Keywords:
Lithium-ion capacitor
Nb_2CT_x MXene
Cation vacancies
T-Nb_2O_5
Reduced graphene oxide

ABSTRACT

Orthorhombic niobium pentoxide (T-Nb_2O_5) is widely acknowledged as a fast pseudocapacitive material. Nevertheless, its application is hindered by the narrow voltage window (1–3 V *vs.* Li/Li^+) that arises from irreversible phase transformation and sluggish kinetics during deep lithiation. Herein, we demonstrate a unique method for introducing Nb vacancies in T-Nb_2O_5 nanoparticles via amine-assisted oxidative etching of Nb_2CT_x MXene, providing extra storage sites and improving structural flexibility by introducing cationic defects. Subsequently reduced graphene oxide (rGO) is employed as substrate to disperse T-Nb_2O_5 nanoparticles and construct T-Nb_2O_5/rGO nanohybrids. Multiple characterizations and computational simulations demonstrate that the resulting T-Nb_2O_5/rGO hybrid anode exhibits rapid and stable multi-electron transfer lithium storage. Owing to the enrichment of Nb vacancies and nanoparticle morphology, even when voltage window of 0.01–3 V (*vs.* Li/Li^+) is extended, T-Nb_2O_5 exhibits a pseudocapacitive mechanism and integrity of partial crystal structure; effectively tackling the structural collapse and sluggish kinetics of T-Nb_2O_5. Consequently, the T-Nb_2O_5/rGO anode shows a superior rate capacity (148 mAh/g at 10 A/g) and cycling stability (3000 cycles at 5 A/g). Remarkably, the assembled lithium-ion capacitors achieve a high energy density of 123.7 Wh/kg, a power density of 22.5 kW/kg, and a capacity retention of 83.6% after 20,000 cycles.

1. Introduction

The gradual replacement of traditional fossil-based energy with renewable energy is the fundamental way to solve the impending energy crisis. Electrochemical energy storage (EES) has become the key supporting technology for the effective utilization of these intermittent and uncontrollable sources (solar, wind, blue energy etc.) [1–6]. Among various EES systems, lithium-ion capacitor (LIC) bridges the performance gap of supercapacitors (high power density) and lithium-ion batteries (high energy density) [7–10]. LIC is generally assembled by a battery-type anode and a capacitor-type cathode in an organic electrolyte, thus possessing advantages of both energy storage mechanisms of supercapacitors and lithium-ion batteries. However, several vital scientific problems of LIC hinder its further development. The most serious challenge is the unbalanced ion kinetics during the lithiation/delithiation process between anode and cathode. The traditional lithium-intercalation anodes often suffer from slow electron transportation and sluggish ion diffusion during lithium storage, impairing high power density, energy density and long-term electrochemical stability of LIC [11–14]. Therefore, current research focuses on the development of anode materials with highly reversible capacity and fast reaction kinetics.

Pseudocapacitive materials exhibit battery-like redox reactions (redox or intercalation pseudocapacitance) on or near the surface. This charge-storage mechanism enables pseudocapacitive materials to display a rapid electrochemical response similar to an electrical double-layer charge storage in capacitive materials [15]. Niobium pentoxide (Nb_2O_5)-based materials are well known for their rich redox chemistry

---

* Corresponding authors at: Institute of Electrical Engineering, Chinese Academy of Sciences, Beijing 100190, China (X. Zhang, Y. Ma).
E-mail addresses: zhangxiong@mail.iee.ac.cn (X. Zhang), wuzs@dicp.ac.cn (Z.-S. Wu), ywma@mail.iee.ac.cn (Y. Ma).

https://doi.org/10.1016/j.cej.2023.143507
Received 23 March 2023; Received in revised form 27 April 2023; Accepted 11 May 2023

(Nb^{5+} to Nb^{+}) [16]. Among Nb_2O_5-based species, orthorhombic niobium pentoxide (T-Nb_2O_5) possesses high rate capability that is enabled by a typical intercalation-based pseudocapacitive behavior. Furthermore, the adjacent niobium atom layers of layered-structure T-Nb_2O_5 with "room and pillar" NbO_6/NbO_7 units are connected by covalent bonds (Nb-O-Nb). This special structure provides a robust lithium-ion diffusion channel and prevents the structural collapse [17–19].

However, the voltage window of T-Nb_2O_5 is generally limited to 1–3 V *vs.* Li/Li^+. In this electrochemical range, the reversible lithiation and delithiation in T-Nb_2O_5 are mainly carried out by solid solution reactions [17], and the theoretical capacity is 202 mAh/g based on $Li_2Nb_2O_5$, *i.e.*, one electron redox per Nb [20–22], When expanding the voltage window to obtain more specific capacity, the intercalation of more than two Li^+ causes the interlayer spacing of T-Nb_2O_5 to increase incessantly, and the amorphized hybrid of NbO, Li_2O, and $Li_xNb_yO_z$ is synchronously separated from $Li_xNb_2O_5$ filled with Li^+ [17]. Although the theoretical capacity of T-Nb_2O_5 is about 400 mAh/g within the 0.01–3 V corresponding to $4Li^+$ per unit [18]. the multi-electron reaction of Nb would not only cause T-Nb_2O_5 sluggish kinetics but also structural collapse (less than 200 cycles *vs* Li/Li^+) [23]. In addition, due to the inherently inferior electric conductivity of Nb_2O_5 (about 3×10^{-6} S/cm), the rate performance of bulk Nb_2O_5 is unsatisfactory during deep lithiation. However, according to the voltage-capacity profile and electrode processes of the LICs (Fig. S1), low anode voltage is good for the full utilization of cathode capacity, increasing the energy density. Currently, strategies such as building rock-salt nanostructure [20], Co/Mn heteroatom doping [17] and oxygen-defect modulation [24] have successfully enabled Nb_2O_5 to work stably in 0.4–3 V. Due to concerns about lithium precipitation on anode and complete destruction of T-Nb_2O_5, the lower cut-off potential (less than 0.4 V) is usually not employed. Moreover, the sluggish electrode kinetics by multi-electron reaction of Nb is still a serious problem. Therefore, the employment of Nb_2O_5 for lithium storage at 0.01–3 V *vs.* Li/Li^+ has been rarely reported and remains highly challenging.

A facile technique to address the above-mentioned problems is defect engineering, which is a desirable strategy to tune the physicochemical performance of functional nanomaterials. Cation vacancy has been proven to provide a thermodynamically favorable driving force for additional cation insertion, thus improving ion storage capacity [25,26]. For instance, the high concentration of iron vacancy in iron oxides has been given credit for reinforced intercalation and conversion capacities for fast lithium storage [27]. Moreover, the vacancy engineering of nanomaterials, especially those with low-dimensional structure, has attracted much attention [28,29]. Compared with 3D solids, the 2D nanosheets, 1D nanowires and 0D quantum dots (QDs) provide a shortened lithium ion transport channel, which alleviates the limitation of lithium-ion solid-state diffusion and exhibits rapid surface-controlled pseudocapacitive electrochemical signature [30–34]. Therefore, within the extended voltage window, the nanostructure design of T-Nb_2O_5 with Nb vacancies and ultrathin nanoparticle morphology is extremely attractive to achieve Nb_2O_5-based anodes with outstanding capacity and high-rate charge storage simultaneously. Currently, several strategies have used MXene (two-dimensional transition metal carbides/nitrides) as the precursor to synthesize MXene-derived metal oxides with various nano-morphologies (such as $Na_2Ti_3O_7$ nanoribbons [35], $NaNbO_3$ nanocubes [36] and T-Nb_2O_5 nanorods [16]). MXene surface carries many termination groups T = (-F, –OH, -O etc.) after hydrofluoric acid (HF) etching from MAX [37–41]. Moreover, MXene has been demonstrated to be defluorinated (-F) in alkaline solution to accelerate oxidation [42–44].

Herein, we have proposed an efficient, controllable, and scalable strategy to innovatively synthesize the QD complexes of isopropylamine (C_3H_9N) with niobic acid (HNb_3O_8) by oxidizing the Nb_2CT_x MXene. C_3H_9N is employed to exfoliate the -F on the surface of MXene, exposing abundant Nb sties, making the oxidation more rapid and synchronous and yielding quantum dot-sized niobate acid (3–5 nm). The oxidized HNb_3O_8 is very easy to age and precipitate, but the QD complexes formed with isopropylamine (IPA-HNb_3O_8) exists stably in the aqueous solution. To maintain the particle size of IPA-HNb_3O_8, graphene oxide (GO) is employed as the substrate material to build the composite system. Subsequently, after calcination, T-Nb_2O_5 nanoparticles are found to be uniformly distributed on the reduced graphene oxide (rGO) to form T-Nb_2O_5/rGO. More importantly, due to the dissolution of Nb in the strong alkali solution, Nb vacancies develop in the T-Nb_2O_5 nanoparticles after oxidative etching [45]. In addition, the coordinate bond in IPA-HNb_3O_8 QDs weakens the interaction of Nb and O, which further increases the concentration of Nb vacancies during the subsequent calcination process [46]. These Nb cation vacancies serve as insertion sites for the storage of additional lithium-ions capacity, and the defects in the crystal structure achieve high structural flexibility, enhancing the structural stability during the process of foreign lithium-ions extraction and insertion [25]. According to the in/ex-situ X-ray diffraction (XRD) and X-ray photoelectron spectroscopy (XPS) analysis, with the conversion from Nb^{5+} to Nb^{+} (0.01–3 V *vs.* Li/Li^+), Nb_2O_5 in T-Nb_2O_5/rGO tends to become amorphous, but part of crystal structure can be retained. Furthermore, density functional theory (DFT) and electrochemical characteristics suggest that the T-Nb_2O_5/rGO still possesses the mechanism of pseudocapacitance and delivers a reduced lithium-ion diffusion barrier. Consequently, the T-Nb_2O_5/rGO delivers a high capacity of 536 mAh/g at 0.2 A/g and a prolonged life span. Moreover, a LIC is assembled with T-Nb_2O_5/rGO anode and activated carbon (AC) cathode. The AC//T-Nb_2O_5/rGO LIC possesses a high energy density of 123.7 Wh/kg at power density of 1.29 kW/kg, and a good capacity retention after 20,000 cycles.

2. Results and discussion

2.1. Characterization of structure and morphology

The fabrication method of IPA-HNb_3O_8 and T-Nb_2O_5/rGO is illustrated in Fig. 1. The MXene Nb_2CT_x is synthesized by etching Al from the Nb_2AlC in HF solution. As shown in Fig. S2, the characteristic peak at 39.0° of Nb_2AlC disappears after HF etching and the (002) peak broadens and downshifts from 12.9° to 7.4°, proving that Nb_2CT_x was successfully prepared [47,48]. Subsequently, Nb_2CT_x powder is immersed in the C_3H_9N aqueous solution and stirred. The black solution transforms into yellow, indicating the complete oxidation of Nb_2CT_x and formation of the IPA-HNb_3O_8 QDs suspension (Fig. S3). This phenomenon is derived from the weakening of interaction between Nb atom of Nb_2CT_x and -F termination group by polar organic amines (C_3H_9N). Nb_2CT_x nanosheets are shredded to form niobic acid nanoparticles through the oxidation reaction, which then chelates with organic amines to form quantum dots that are stable in aqueous solution. To prevent IPA-HNb_3O_8 QDs from agglomerating, GO is used as the substrate to construct a composite precursor (IPA-HNb_3O_8/GO). Finally, the IPA-HNb_3O_8/GO is annealed in Ar to form the T-Nb_2O_5/rGO.

Fig. 2a shows the XRD patterns of Nb_2CT_x reacting in isopropylamine aqueous solution for different time periods (0–24 h). The first stage of reaction takes place between 0 and 9 h, with the intercalation of isopropylamine cations (IPA^+) into the Nb_2CT_x interlayer space by electrostatic interaction. The shift of (002) peak of Nb_2CT_x from 7.51° to 5.88° verifies the intercalation of IPA^+. Calculated by the Bragg equation ($2d\sin\theta = n\lambda$), the d-spacing of Nb_2CT_x is enlarged to about 1.54 nm [37,49]. Other stages of reaction are between 12 and 24 h, mainly the oxidation process of Nb_2CT_x. Although one characteristic peak of HNb_3O_8 appears after 3 h, most of the other peaks are visible after 9 h and the intensity increases with time, indicating that the oxidation of Nb_2CT_x has an obvious acceleration stage. The precipitates that are separated from the reaction solution can provide a more intuitive way to observe the accelerated oxidation process. As shown in Fig. S4, the color of the precipitate rapidly changes from black to gray between 9 and 12

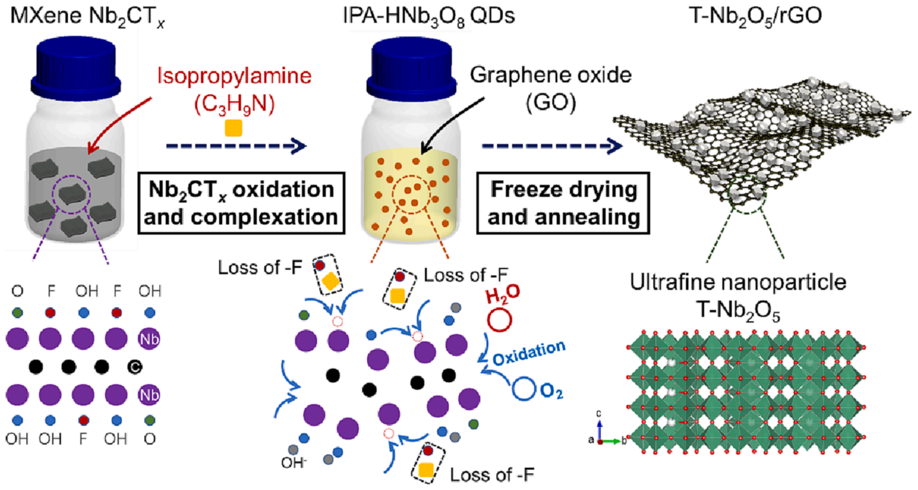

Fig. 1. Schematic illustration of the fabrication process of IPA-HNb_3O_8 QDs and T-Nb_2O_5/rGO.

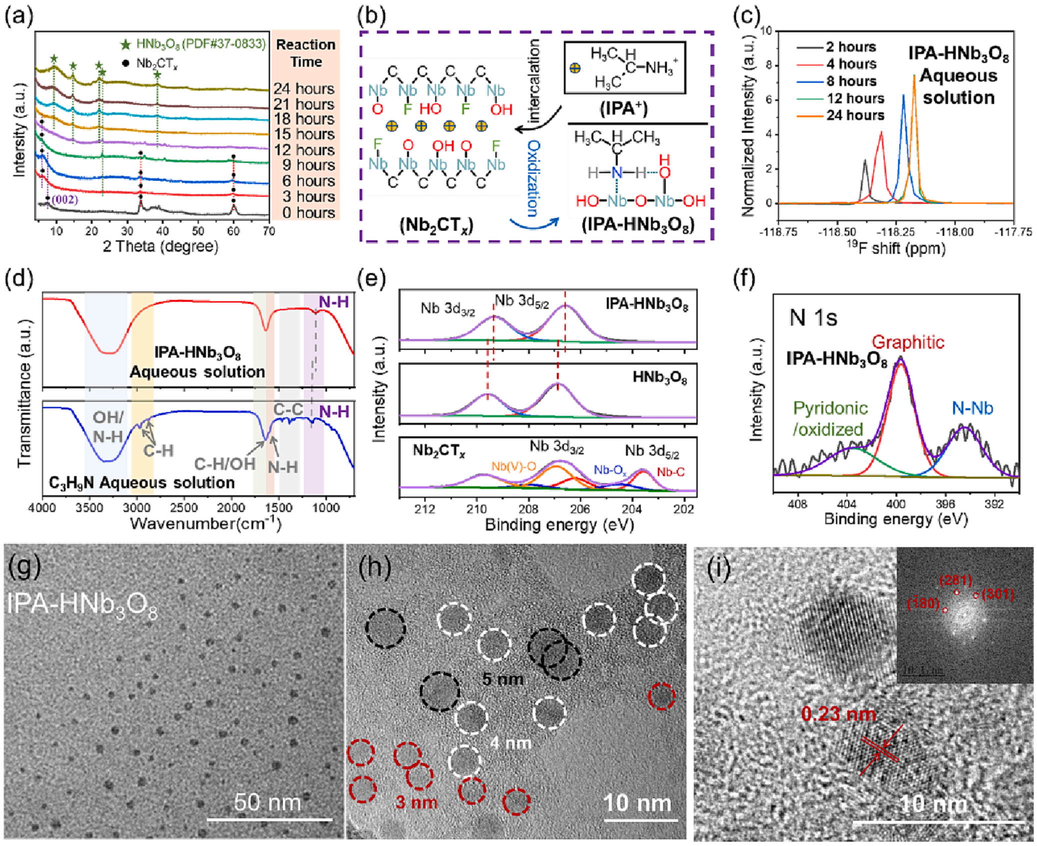

Fig. 2. Structural, morphological, and compositional characterizations of IPA-HNb_3O_8. a) XRD patterns of Nb_2CT_x oxidized in C_3H_9N aqueous solution for different time periods. b) Schematic diagram for intercalation and oxidation process of Nb_2CT_x. c) ^{19}F HMR spectrum of IPA-HNb_3O_8 aqueous solution for different time periods. (d) FT-IR curves of IPA-HNb_3O_8 and C_3H_9N aqueous solution. e and f) High-resolution XPS spectra of Nb 3d and N1s of Nb_2CT_x and IPA-HNb_3O_8 and HNb_3O_8. g) Typical TEM images of IPA-HNb_3O_8. h and i) HRTEM of IPA-HNb_3O_8 (inset of i: SAED pattern).

h. The oxidation process of Nb_2CT_x begins at the edges and accelerates as more Nb sites are exposed on the surface of Nb_2CT_x. This is accompanied by a gradual reduction in the size of Nb_2CT_x and a transformation of the surface from smooth to rough, ultimately resulting in the formation of flocculent HNb_3O_8. Notably, the supernatant obtained from the separation of niobic acid precipitation after the complete oxidation of Nb_2CT_x in C_3H_9N aqueous solution has a strong Tyndall effect (Fig. S5a). After adding HCl, white flocs are precipitated (Fig. S5b), which proves that the Tyndall effect comes from the complex formed by HNb_3O_8 and C_3H_9N, indicating that the solution has colloidal properties. In contrast, in the NaOH aqueous solution of the same pH value (12.31), due to the absence of organic ligands, the oxidized Nb_2CT_x directly forms HNb_3O_8 and rapidly ages, so there is no Tyndall effect (Fig. S5c). Therefore, during the oxidation process of Nb_2CT_x, it is reasonable to believe that HNb_3O_8 and IPA^+ can construct supramolecular structures through chelation effect and electrostatic interaction (Fig. 2b) [50,51]. Moreover, the accelerated oxidation phenomenon is related to the massive and simultaneous detachment of -F from the surface of MXenes. There is sufficient evidence that MXene can form the corresponding fluoride in an alkaline environment. The detailed reactions of Nb_2CT_x in alkaline solution are listed in the supporting information as Reaction S1 to S3 [42].

According to the nuclear magnetic resonance (NMR) results of IPA-HNb_3O_8 aqueous solution, only one ^{19}F peak appears around 118 ppm, which is consistent with the position of ^{19}F peak in the pristine NH_4F aqueous solution (Fig. S6). Furthermore, as the reaction progresses, as shown in Fig. 2c, the low-field shift of ^{19}F signal and the gradual increase of peak intensity indicates that the -F termination group is gradually ionized, which increases its content. The same phenomenon can also occur in the NaOH aqueous solution (with the same pH value), but the ^{19}F peak is shifted to high-field by -0.91 ppm, which is related to the cation's species (Na^+ or IPA^+) bound to F^-(Fig. S7a) [52,53]. In addition, the F content in NaOH aqueous solution is lower than IPA-HNb_3O_8 aqueous solution at each time stage (Fig. S7b and S7c), and according to XRD patterns in Fig. S7d, the oxidation of Nb_2CT_x in NaOH aqueous solution is not obvious, indicating that C_3H_9N can accelerate the detachment of -F and oxidation of Nb_2CT_x. Subsequently, various MXenes were tested in C_3H_9N aqueous solution, and it was found that the sample with the highest F content gets oxidized the fastest (Fig. S7e and S7f). On one hand, the F content can directly affect the oxidation rate of Nb_2CT_x. On the other hand, the strong polarity of C_3H_9N enables the rapid conversion of highly electronegative F into F^- and its detachment from Nb_2CT_x surface through hydrogen bonding. The Nb_2CT_x with more metal sites exposed will undergo multi-origin and simultaneous oxidation, which becomes the basis for the preparation of HNb_3O_8 quantum dots.

Fig. 2d displays the Fourier transform infrared (FT-IR) spectra, compared with original C_3H_9N aqueous solution, the N-H torsion vibration around 1200 cm^{-1} shifts toward lower frequency in IPA-HNb_3O_8 aqueous solution [54,55]. The red shift of FT-IR band indicates that the bond order and structure order of N have changed, which might result from the chemical bonding action between Nb and N atom [51,56]. XPS is employed to further reveal the chemical constituent and bonding state of IPA-HNb_3O_8 complex. Fig. 2e shows the Nb 3d spectrums of Nb_2CT_x, HNb_3O_8 and IPA-HNb_3O_8. The peaks located at 203.65 (Nb $3d_{3/2}$) and 206.67 eV (Nb $3d_{5/2}$) confirm the presence of Nb-C originating from the Nb_2CT_x, and other peaks correspond to the Nb-O_x bond (204.8 and 207.6 eV) and Nb(V) (206.8 and 209.6 eV) in the Nb_2CT_x, respectively [36]. After the reaction of C_3H_9N, Nb in the aged precipitated HNb_3O_8 gets oxidized to the highest valence state (Nb^{5+}). The original Nb-C bond is cleaved, resulting in the conversion of a portion of the C into CH_4, CO, CO_2 and other gaseous products that escape, while some C remains in the solution as amorphous carbon [57]. The Nb binding energy of IPA-HNb_3O_8 is slightly lower than that of HNb_3O_8 by ~ 0.3 eV, which is due to the increase of electron density caused by N substituting for O around the Nb atom [50,58]. In N 1 s XPS spectrum of IPA-HNb_3O_8, the peak at 399.9 eV corresponds to C-N, another peak located at 402–405 eV is assigned to the various oxidized nitrogens. Notably, an obvious peak is observed at the low energy of 395.1 eV, which is attributed to the chemical interaction between Nb and N [59,60]. However, no N 1 s peak is observed at 395.1 eV in the HNb_3O_8, and the only peak at 399.9 eV is from residual C_3H_9N in the precipitate (Fig. S8). The XPS results suggest that it is the organic–inorganic coordination compounds obtained by oxidation of Nb_2CT_x and C_3H_9N through hydrogen bonds and Nb-N bonds, which disperse the IPA-HNb_3O_8 QDs stably in aqueous solution.

Transmission electron microscopy (TEM) was used to gain insight on the microstructure of IPA-HNb_3O_8 QD, as displayed in Fig. 2g and S9. The IPA-HNb_3O_8 QDs are uniform ultrasmall particles. In addition, some amorphous carbon residues from MXene oxidation can also be observed. From the high-resolution TEM (HRTEM) images in Fig. 2h and 2i, the lateral sizes of QDs are uniform, ranging from 3 to 5 nm. The lattice fringes of 0.23 nm are clearly visible, consistent with the (3 0 1) crystal planes of HNb_3O_8. In addition, the fast Fourier transform pattern can also confirm the orthorhombic HNb_3O_8. Fig. S10 a-d present the electron probe micro-analyzer (EPMA) map scanning results of O, Nb and N in IPA-HNb_3O_8. The detected N element verifies the XPS result, which confirms the existence of organic–inorganic coordination compounds consisting of isopropylamine and HNb_3O_8. In contrast, the HNb_3O_8 obtained by completely oxidizing Nb_2CT_x in NaOH aqueous solution could not be stably dispersed in the solution. As shown in the Fig. S11, HNb_3O_8 does not form the coordination compounds in aqueous NaOH, but agglomerates into large particles with a lateral size of more than 50 nm.

Using HNb_3O_8 as precursor, TT-Nb_2O_5 (pseudohexagonal), T-Nb_2O_5 (orthorhombic) M-Nb_2O_5 (tetragonal) and H-Nb_2O_5 (monoclinic) can be obtained by adjusting the heating temperature from 650 to 900 ℃ (Fig. S12) [21]. Among them, T-Nb_2O_5 is demonstrated to have the best rate capability and is used in LICs [16,50,61]. To obtain T-Nb_2O_5 nanoparticles, graphene oxide (GO) is employed as substrate to prevent IPA-HNb_3O_8 QDs from agglomeration during calcination at 800 ℃. The physicochemical properties of T-Nb_2O_5/rGO were also systematically investigated. According to the results of thermogravimetric analysis (TGA), the T-Nb_2O_5/rGO-n (n represents the approximately mass ratio of T-Nb_2O_5 and rGO) is successfully prepared (Fig. S13a to S13c). The XRD patterns of T-Nb_2O_5/rGO-4 is displayed in Fig. 3a. The typical diffraction peaks at $\approx 22.6^\circ$, 28.4°, 36.6°, 46.2, and 55.1° are indexed as the (0 0 1), (1 8 0), (1 8 1), (0 0 2) crystal plane of orthorhombic T-Nb_2O_5 (JPDS Card No. #30-0873), respectively. The diffraction peak of rGO located at 26.0° is shown in T-Nb_2O_5/rGO-4 [62,63] and the intensity increases with its content (Fig. S14).

The SEM image in Fig. S15a clearly shows that IPA-HNb_3O_8 loaded on GO displays a uniform dispersion of QD on nanosheets with only a few agglomerations. Conversely, IPA-HNb_3O_8 without a substrate forms nanospheres that subsequently agglomerate into blocks (Fig. S15b and S15c). After heating at 800 ℃, the two-dimensional structure of rGO remains largely intact, and the nanoparticles anchor on the surface of rGO (Fig. 3b and S16a). As the proportion of IPA-HNb_3O_8 precursor increases, the T-Nb_2O_5 nanoparticles start to agglomerate and the rGO begins to curl (Fig. S16b to S16d). Excessive rGO loading is not conducive to the pseudocapacitive properties of T-Nb_2O_5. For T-Nb_2O_5/rGO-4, despite the increase in particle size of the IPA-HNb_3O_8 QDs due to the thermal shrinkage of graphene, the size of T-Nb_2O_5 remains uniformly below 50 nm (Fig. 3c). Furthermore, TEM images in Fig. 3d confirm that T-Nb_2O_5 is uniformly distributed on the rGO surface, which is consistent with the SEM results. It can be observed from the high-angle annular dark-field scanning transmission electron microscopy (HADDF-STEM) images that there are many pits on the surface of T-Nb_2O_5 (Fig. 3e), which may be caused by the agglomeration of IPA-HNb_3O_8 QDs during the calcination process. Fig. 3f displays a clear lattice fringe of 0.393 nm, consistent with the (0 0 1) crystal planes of T-Nb_2O_5 [21]. In addition, the atomic column intensity variation relates to the atomic occupations, which enables direct visualization of Nb vacancies. The energy dispersive X-ray spectroscopy (EDS) mapping confirms that Nb, O, C are homogeneously distributed in the T-Nb_2O_5/rGO-4 (Fig. 3g). Uniformly dispersed T-Nb_2O_5 nanoparticles are beneficial for fast Li^+ storage and release. The Nb vacancies can serve as additional storage sites to improve anode capacity. Moreover, the defects in the crystal structure greatly improve structural flexibility, resulting in better structural stability during the extraction and insertion of foreign ions [25]. The unique two-dimensional structure of rGO provides more intimate connection and thus improves the conductivity of metal oxide composite, so T-Nb_2O_5/rGO-4 has the potential as an anode material for LICs.

2.2. Electrochemical performance and lithium storage mechanism

To demonstrate the positive effects of the unique material tailoring, electrochemical performance of as-prepared T-Nb_2O_5/rGO is investigated in the half-cell between the potential range of 0.01–3.0 V (*vs* Li/Li^+). The cyclic voltammetry (CV) of T-Nb_2O_5/rGO-4 at a sweep rate of 0.2 mV/s is displayed in Fig. 4a. Two reduction peaks are centered at 1.78 and 1.54 V during the initial discharge, which corresponds to two Li^+ insertion in one Nb_2O_5 unit to form $Li_2Nb_2O_5$ [17,64]. When the voltage reaches 0.81 V, a new lithiated phase is formed. Subsequently, the deep lithiation causes the phase segregation from Li stuffed $Li_xNb_2O_5$ to amorphized hybrid of NbO, Li_2O, and $Li_xNb_yO_z$ [65]. The corresponding anodic peak appears near 2.11 V. When the voltage window is

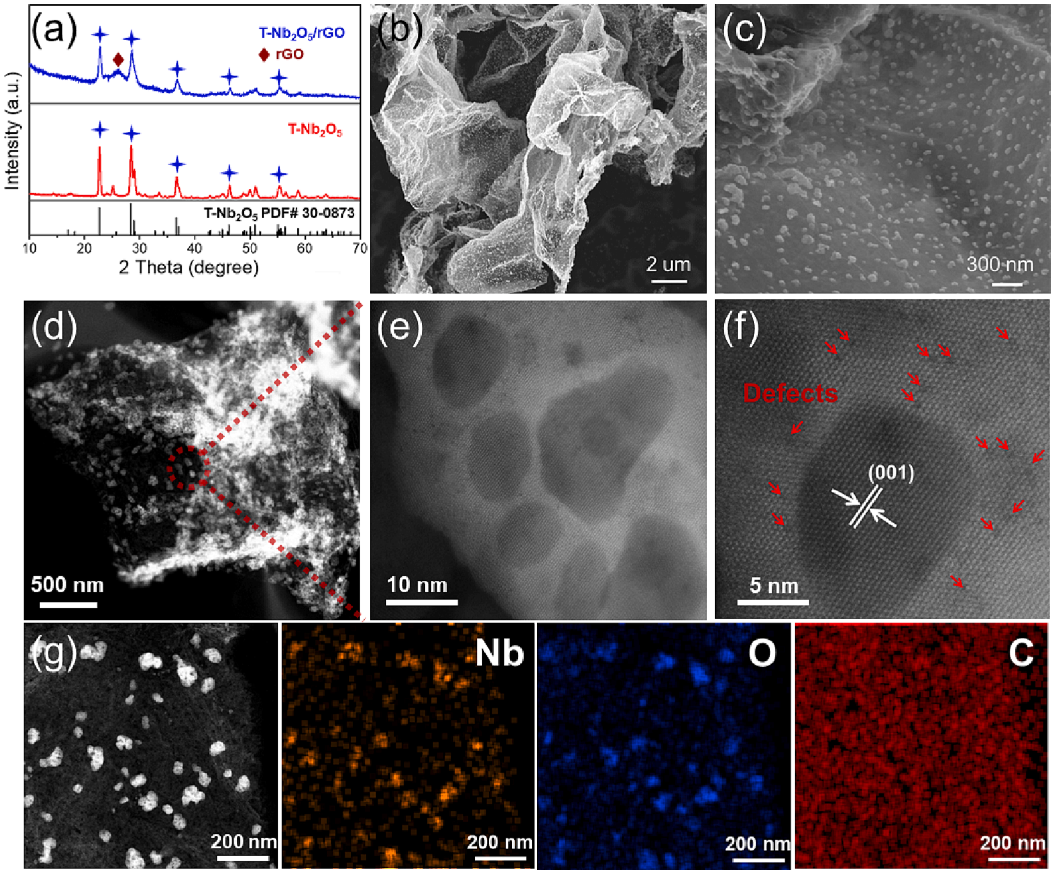

Fig. 3. Structural morphological and compositional characterizations of T-Nb_2O_5/rGO-4. a) XRD patterns of T-Nb_2O_5 and T-Nb_2O_5/rGO-4. b and c) SEM images of T-Nb_2O_5/rGO-4. d and f) HADDF-STEM images of T-Nb_2O_5/rGO-4 at different magnifications. g) Low-magnification STEM images of T-Nb_2O_5/rGO and EDS mapping.

limited to 1 ~ 3 V, the peak at 2.11 V does not appear because there is no phase transition of Nb_2O_5 (Fig. S17). And another reduction peak at 0.51 V is attributed to the formation of solid electrolyte interphase (SEI) layers and other irreversible reaction in the electrolyte. In the subsequent cycle, a pair of redox peaks are centered at 1.63 and 1.91 V, respectively, which is assigned to the reversible conversion between Nb^{5+} and Nb^{4+}. The CV curves of T-Nb_2O_5/rGO-4 are much more reversible compared with pristine T-Nb_2O_5 (Fig. S18a). From Fig. S18b, in the first cycle of galvanostatic charge/discharge (GCD) profiles of T-Nb_2O_5/rGO-4, a remarkable potential plateau can be observed at 0.8 V, which corresponds to the irreversible phase transition of T-Nb_2O_5. The initial charge/discharge capacity of the T-Nb_2O_5/rGO-4 is 581/873 mAh/g with a 66.6% coulombic efficiency (CE). The initial irreversible capacity loss is caused by the formation of SEI and irreversible reaction. The subsequent GCD profiles of T-Nb_2O_5/rGO-4 remain basically unchanged and highly symmetric. Moreover, there is no obvious platforms in the profiles, which proves that T-Nb_2O_5/rGO has a pseudocapacitance-based energy storage mechanism [1,15,30].

Since one of the main purposes of this nanomaterial is to improve the sluggish kinetics, the rate capability of T-Nb_2O_5/rGO-n was surveyed (Fig. 4b) at different current densities to demonstrate the claimed benefits. Compared with pristine T-Nb_2O_5 and rGO (Fig. S19a and S19b), T-Nb_2O_5/rGO-4 delivers excellent rate capability of 536, 424, 381, 320, 285, 238 and 182 mAh/g at current density of 0.2, 0.5, 1, 2, 3, 5 and 8 A/g, respectively. Importantly, even at 10 A/g, the T-Nb_2O_5/rGO-4 can retain 148 mAh/g, superior to that of T-Nb_2O_5/rGO-3 (68 mAh/g) and T-Nb_2O_5/rGO-5 (80 mAh/g). The rapidly declining rate capability of T-Nb_2O_5/rGO-3 and T-Nb_2O_5/rGO-5 could be ascribed to the low load or agglomeration of T-Nb_2O_5 respectively, resulting in inferior Li^+ diffusion rate. Once the current density is set back to 0.2 A/g, the recovered capacity of 539 mAh/g for T-Nb_2O_5/rGO-4 indicates its reversible lithium storage behavior. Furthermore, the cycling performance of T-Nb_2O_5/rGO-4 and T-Nb_2O_5 (after testing of rate capability) are investigated at 5 A/g over 3000 cycles (Fig. 4c). The reversible capacity of T-Nb_2O_5/rGO-4 electrode can reach 160 mAh/g, superior to pristine T-Nb_2O_5 (24 mAh/g). It is obvious that the capacity of bulk T-Nb_2O_5 drops rapidly after several cycles, and the structural damage caused by phase transition directly results in the attenuation of electrochemical performance. Compared with previous studies about T-Nb_2O_5-based materials for lithium storage (Table S1) the operating voltage window of T-Nb_2O_5/rGO-4 is extended to 0.01–3.0 V which increased the capacity, but is not detrimental to rate capability and cycle life. The rGO substrate not only provides robust binding sites for T-Nb_2O_5 nanoparticles, but also mitigates stress of T-Nb_2O_5 during lithiation process. Moreover, the widely distributed Nb vacancies in T-Nb_2O_5 provides more insertion sites for the lithium-ion, and the uniformly dispersed nanoparticle size allows T-Nb_2O_5 to fully contact with electrolyte and greatly shorten the Li^+ transmission channel, allowing the composite to have a faster kinetics response speed. These observations add further credence to the potential of T-Nb_2O_5/rGO-4 as anode materials of LICs.

To get clear insights into lithium storage mechanism of T-Nb_2O_5/rGO-4, CV tests were performed at various sweep rates is carried out. CV curves at sweep rates ranging from 0.2 to 5 mV/s retain a similar shape (Fig. S20), which indicates that T-Nb_2O_5/rGO-4 has high stability and reversibility. Generally, the energy storage behavior can be plotted by dependence of peak current (i) and sweep rate (v). The i and v follow the relationship of $i = av^b$. The b value of 0.5 and 1 represent ideal diffusion-controlled and capacitive controlled mechanism, respectively [66,67]. The inset in Fig. 4d presents b values of 0.77 and 0.85 for anodic and cathodic peaks respectively, illustrating that the lithium storage behavior of T-Nb_2O_5/rGO-4 is dominated by surface-controlled (capacitive contribution). Quantitatively, the capacitive contribution

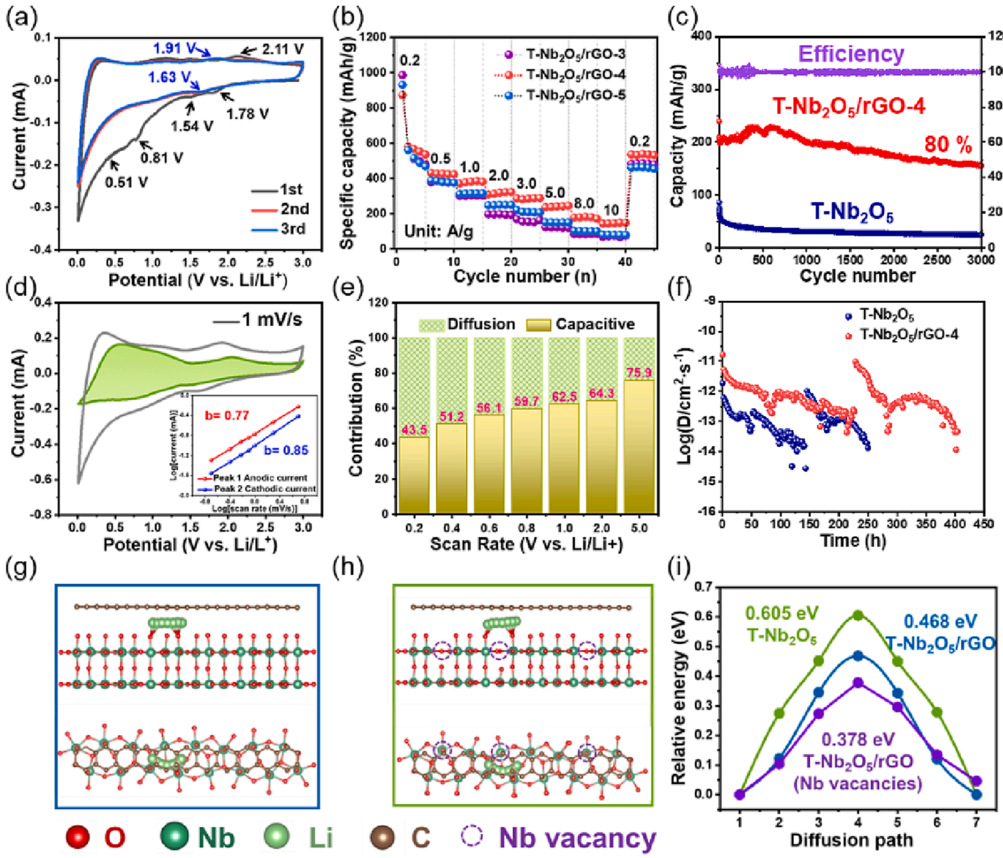

Fig. 4. Electrochemical performance of T-Nb_2O_5/rGO. a) CV plots at a scan rate of 0.2 mV/s in the initial 3 cycles. b) Rate performance with different mass ratios. c) Cycle performance. d) Capacitive-controlled contributions (green section) at 1 mV/s and the inset is the corresponding log(i) versus log(v) plots of cathodic and anodic peaks. e) The capacity contribution ratios at various scan rates. f) The diffusion coefficients D_{Li}. g-h) DFT simulation of lithium-ion diffusion path within T-Nb_2O_5/rGO heterostructures with and without Nb vacancies. i) Diffusion energy battier of lithium-ion in T-Nb_2O_5, T-Nb_2O_5/rGO without defect and T-Nb_2O_5/rGO with Nb vacancies. (For interpretation of the references to color in this figure legend, the reader is referred to the web version of this article.)

is calculated based on formula of $i = k_1v + k_2v^{1/2}$ [37,50]. According to Fig. 4d, the capacitive ratio in the T-Nb_2O_5/rGO-4 can achieve 62.5% at 1 mV/s. As the sweep rate increases, the capacitive contribution ratio improves (Fig. 4e), indicating that T-Nb_2O_5/rGO-4 possesses fast Li^+ transport kinetics and rate capability. In contrast, as shown in Fig. S21, pristine T-Nb_2O_5 anode delivers a sluggish Li^+ storage mechanism dominated by diffusion-controlled contribution. The multi-electron reaction of Nb causes the extremely sluggish lithium-ion diffusion in T-

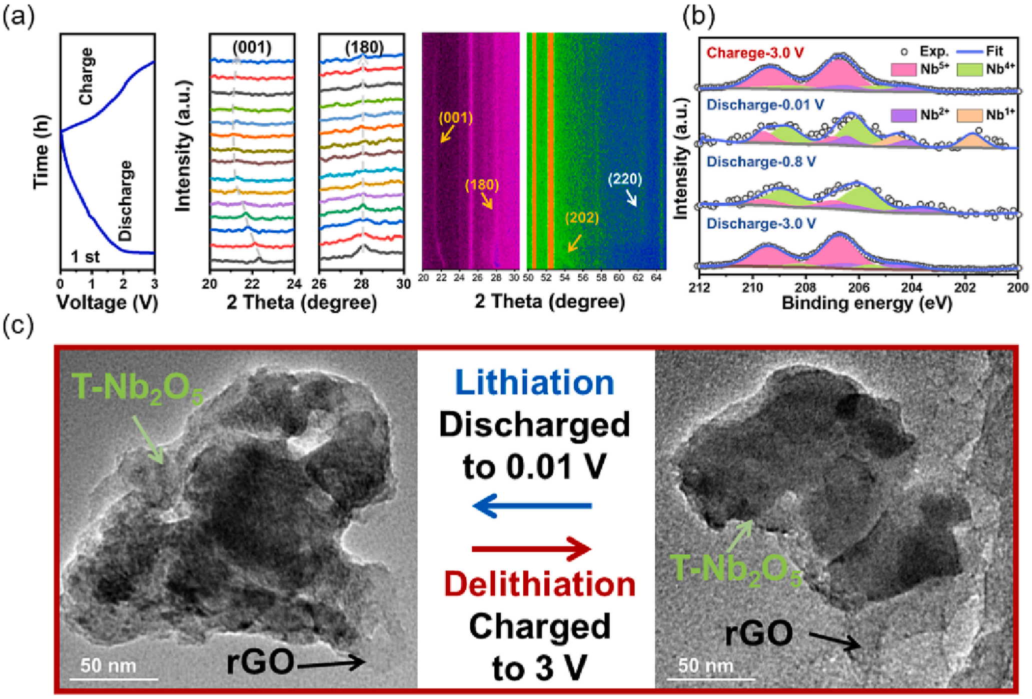

Fig. 5. A) in-situ XRD patterns of T-Nb_2O_5/rGO-4 electrode during the first charge/discharge process. b) Ex-situ XPS profiles of Nb 3d under various states. c) TEM images of T-Nb_2O_5/rGO-4 during the initial cycle at various states.

Nb_2O_5 bulk. But the T-Nb_2O_5 nanoparticles with abundant Nb vacancies provides short ion transport channels and larger pseudocapacitive contribution. Galvanostatic intermittent titration technique (GITT) is employed to further investigate the lithium-ion storage kinetics of T-Nb_2O_5/rGO-4. From Fig. 4f, the calculated lithium-ion diffusion coefficients during the charge/discharge of T-Nb_2O_5/rGO-4 are higher than pristine T-Nb_2O_5, indicative of the rapid Lithium-ion diffusion rate of T-Nb_2O_5/rGO-4. The first-principles calculation based on DFT method are employed to analyze the diffusion barriers of lithium-ion in T-Nb_2O_5, T-Nb_2O_5/rGO and T-Nb_2O_5/rGO with Nb vacancies. According to Fig. 4g-i and S22, the energy barriers for interfacial diffusion of T-Nb_2O_5/rGO without vacancies (0.468 eV) is lower than that in T-Nb_2O_5 (0.605 eV). Significantly, the T-Nb_2O_5/rGO with abundant Nb vacancies is observed to deliver the lowest diffusion barrier (0.378 eV). These simulation results show an improved kinetics of Li^+ diffusion in T-Nb_2O_5/rGO-4, which is consistent with the GITT test results.

In-situ XRD and ex-situ XPS are carried out to analyze the structural evolution and Nb 3d conversion mechanism of T-Nb_2O_5/rGO-4. As shown in Fig. 5a, the in-situ XRD patterns of first discharge and charge cycle is recorded, and the corresponding voltage profiles are shown on the left. In the discharge process, the (0 0 1) and (2 0 2) peaks at 22.5° and 55.1° gradually shift to lower angles. These peak shifts are caused by the lattice expansion as the degree of lithiation progresses. In the following charge process, the peak of (0 0 1) shifts reversibly towards high angle but intensity gradually weakens, indicating the irreversible amorphization of T-Nb_2O_5/rGO-4. Moreover, deep lithiation triggers a multi-electron reaction in Nb. This process causes the segregation of NbO and Li_2O domains from $Li_2Nb_2O_5$ phase and results in the formation of amorphous $Li_xNb_yO_z$. In the corresponding contour plots of in-situ XRD curves, a new peak at 62.5° appears when the voltage drops below 1 V, corresponding to the (2 2 0) planes of NbO. In the subsequent electrochemical behavior, the NbO will be used as a conductive wire to promote the cycle stability of $Li_xNb_yO_z$. In the in-situ XRD curves of third discharge and charge cycle (Fig. S23), the (0 0 1) peak becomes gradually broader and finally vanish, but the (1 8 0) peak at 28.4° can still be observed from the first to third cycles. It appears that the amorphous $Li_xNb_yO_z$ partially retains the structure of T-Nb_2O_5. This may be due to the high structural flexibility and stability achieved by the abundant Nb defects, which ensures a good cycle life of T-Nb_2O_5/rGO-4 anodes. Fig. 5b is the ex-situ XPS tests result of Nb 3d at different lithiation depths. At the pristine 3.0 V (start of third cycle), T-Nb_2O_5/rGO-4 shows $Nb_{3/2}$ and $Nb_{5/2}$ peaks at 209.6 and 206.8 eV, corresponding Nb^{5+}. In addition, the peak of Nb^{2+} at 206.5 and 203.6 eV are also observed, which comes from the irreversible NbO generated in the first cycle. Upon discharging to 0.8 V, the shift of Nb 3d peak to 208.5 and 205.7 eV suggests the reduction from Nb^{5+} to Nb^{4+}. Then, the proportion of Nb^{2+} increases with deep discharge to 0.01 V, and two new peaks located at 204.6 and 201.8 eV are observed, which is slightly lower than Nb^+ (205.4 and 202.6 eV). These results suggest that some suboxides not present in T-Nb_2O_5/rGO-4 is formed, which proves that the Nb has experienced a lager reduction. Subsequently, charging back to 3.0 V, the T-Nb_2O_5/rGO-4 returns to Nb^{5+}. The content of residual Nb^{4+} and Nb^{2+} are almost the same as that before discharge. The ex-situ XPS results validate that the Nb element in T-Nb_2O_5/rGO-4 undergoes reversible multi-electro transfer during charge and discharge.

Minimal morphological variations are observed in T-Nb_2O_5/rGO-4 after rate performance and durability testing. As the number of charge and discharge cycles increase, the thickness of the SEI film increases. However, the two-dimensional structure of T-Nb_2O_5/rGO-4 remains intact (Fig. S24). TEM images of T-Nb_2O_5/rGO-4 in Fig. 5c at different lithiation states, show that after the initial discharge to 0.01 V, T-Nb_2O_5 changes to amorphous state and experiences a slight volume expansion due to complete lithiation. Subsequently, with the charging to 3 V, the T-Nb_2O_5 nanoparticle finally returns to its original morphology, showcasing excellent reversibility and stability of T-Nb_2O_5/rGO-4. The reversible conversion of T-Nb_2O_5/rGO-4 in the 0.01–3 V voltage window indicates that T-Nb_2O_5 still maintain good cycle stability after undergoing deep lithiation.

2.3. Lithium-ion capacitor (LIC) based on AC cathode and T-Nb_2O_5/rGO

To demonstrate practical application, a LIC full-cell was prepared using T-Nb_2O_5/rGO-4 as anode and commercial activated carbon (AC, YP80F) as cathode (Fig. 6a). The AC exhibits a typical capacitive characteristic and has potential as cathode for LICs (Fig. S25). Prior to assembling the LIC, to eliminate the irreversible capacity and adjust the potential of anode, the T-Nb_2O_5/rGO-4 anode is prelithiated by charging and discharging from 0.01 to 3 V (*vs.* Li/Li^+) for 3 cycles at 0.2 A/g. To balance the different capacities of T-Nb_2O_5/rGO-4 anode and AC cathode, we optimized the mass ratio as 2:1 to obtain the maximum energy and power output of the LIC (Fig. S26). Base on the principle that cathode cannot be over-oxidized and no lithium precipitation occurson the anode, we expanded the working window as much as possible to harvest the maximum energy density and power density. As shown in Fig. 6b, the CV curves of AC//T-Nb_2O_5/rGO-4 LIC in a voltage window of 1–4.2 V are nearly rectangular even at 200 mV/s, without distinct deviation or polarization, indicating excellent reversibility and rate capability. Fig. 6c is the GCD profiles of LIC, due to different charge storage behaviors of anode and cathode, the profiles exhibit the symmetric and near-linear slopes with a slight curvature at different current densities from 0.2 to 20 A/g. The specific capacitance of the LIC is calculated based on the total mass of active materials, including both the anode and cathode. From Fig. 6d, the LIC achieves 55.36 F/g at 0.2 A/g. And even the current density increases to 10 A/g, the LIC also retains 17.20 F/g. Ragone plot obtained from GCD text shows that the LIC delivers an energy density of 123.7 Wh/kg at power density of 1.29 kW/kg and maximum power density of 22.5 kW/kg at energy density of 34.4 Wh/kg, as shown as Fig. 6e. This result is superior to many previous reported LIC devices [16,50,68–71], such as ACN//3D-CNWs/TNb_2O_5 [69], AC//N-NbOC [50], AC//T-Nb_2O_5 [16], and AC//NRC [70]. Moreover, AC//T-Nb_2O_5/rGO-4 LIC presents an excellent cycling stability with a capacitance retention of 83.6% after 20,000 cycles at 5 A/g and the coulombic efficiency remains nearly 100% throughout (Fig. 6f). This work clearly elucidates an enhancement in the overall electrochemical performance compared with previous studies pertaining to Nb_2O_5-based materials used in LICs (Table S2). This innovative structural design of T-Nb_2O_5/rGO-4 circumvents the main intrinsic drawbacks of kinetics of LICs anode materials and carbon-based cathode.

3. Conclusions

In summary, an oxidative etching route is proposed to prepare IPA-HNb_3O_8 (metal oxide) QDs by using Nb_2CT_x (MXene). Isopropylamine causes the abscission of -F on the surface of Nb_2CT_x, accelerates the oxidation and forms complex QDs with niobic acid through chelation effect. Subsequently, T-Nb_2O_5/rGO composite is prepared, in which T-Nb_2O_5 nanoparticles with Nb vacancies is uniformly distributed on the surface of rGO. This innovative material design and synthesis strategy extends the operating voltage window of Nb_2O_5-based materials to 0.01–3 V achieving impressive reversible capacity (536 mAh/g at 0.2 A/g) and extraordinarily stable cycling performance (80% over 3000 cycles). The expanded voltage window improves the specific capacitance, the enrichment of Nb defects endows T-Nb_2O_5/rGO with predominantly pseudocapacitive contribution, and the ultra-fine nanoparticles ensure fast reaction kinetics. Furthermore, the stability is attributed to the fact that despite amorphization, underlying structure of T-Nb_2O_5/rGO remains stable. To combine all the advantages, a LIC was assembled with AC cathode and T-Nb_2O_5/rGO-4 anode, which showed an energy density of 123.7 Wh/kg at power density of 1.29 kW/kg and long cycling stability (83.6 % over 20,000 cycles). Although the theoretical capacity of Nb_2O_5 is not the highest, with the increasing variety of MXenes, this strategy of synthesizing metal oxides with special nanostructure through

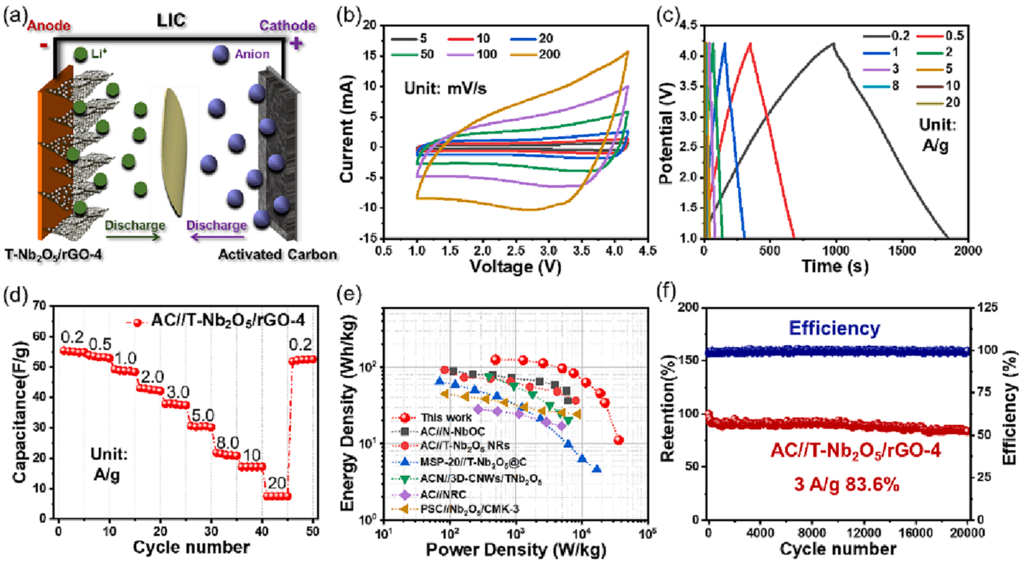

Fig. 6. Electrochemical performance of AC//T-Nb_2O_5/rGO-4 LIC. a) Schematic diagram of discharge mechanism of LIC. b) CV plots at various sweep rates. c) GCD profiles at current densities of 0.2–20 A/g and d) corresponding capacitance versus cycle number. e) Ragone plot compared with other Nb_2O_5-based LIC devices reported. f) Long-term cycling stability of the LIC at 3 A/g for 20 000 cycles.

oxidation holds great potential in the field of energy storage materials.

Declaration of Competing Interest

The authors declare that they have no known competing financial interests or personal relationships that could have appeared to influence the work reported in this paper.

Data availability

Data will be made available on request.

Acknowledgments

This work was financially supported by the National Natural Science Foundation of China (Nos. 52077207, 52002396, 51907193 and 51677182), the Key Research Program of Frontier Sciences, CAS (No. ZDBS-LY-JSC047), the Youth Innovation Promotion Association CAS (No. 2020145).

Appendix A. Supplementary data

Supplementary data to this article can be found online at https://doi.org/10.1016/j.cej.2023.143507.

References

[1] P. Simon, Y. Gogotsi, Perspectives for electrochemical capacitors and related devices, Nat. Mater. 19 (11) (2020) 1151–1163.

[2] F. Xing, Z. Bi, F. Su, F. Liu, Z.-S. Wu, Unraveling the design principles of battery-supercapacitor hybrid devices: from fundamental mechanisms to microstructure engineering and challenging perspectives, Adv. Energy Mater. 12 (26) (2022) 2200594.

[3] J. Pang, B. Chang, H. Liu, W. Zhou, Potential of MXene-based heterostructures for energy conversion and storage, ACS Energy Lett. 7 (1) (2022) 78–96.

[4] Y. Sun, N. Liu, Y. Cui, Promises and challenges of nanomaterials for lithium-based rechargeable batteries, Nat. Energy 1 (2016) 16071.

[5] Y. Gao, L. Zhao, Review on recent advances in nanostructured transition-metal-sulfide-based electrode materials for cathode materials of asymmetric supercapacitors, Chem. Eng. J. 430 (2022), 132745.

[6] G. Li, X. Guan, A. Wang, C. Wang, J. Luo, Cations and anions regulation through zwitterionic gel electrolytes for stable lithium metal anodes, Energy Storage Mater. 24 (2020) 574–578.

[7] K. Zou, P. Cai, X. Deng, B. Wang, C. Liu, J. Li, H. Hou, G. Zou, X. Ji, Revealing dual capacitive mechanism of carbon cathode toward ultrafast quasi-solid-state lithium ion capacitors, J. Energy Chem. 60 (2021) 209–221.

[8] L. Wang, X. Zhang, C. Li, X.-Z. Sun, K. Wang, F.-Y. Su, F.-Y. Liu, Y.-W. Ma, Recent advances in transition metal chalcogenides for lithium-ion capacitors, Rare Met. 41 (9) (2022) 2971–2984.

[9] Z. Yuan, S. Ju, W. Li, H. Guo, K. Chen, M. Yue, X. Yu, Y. Wang, Alkali ions pre-intercalated 3D crinkled Ti3C2Tx MXene architectures for advanced sodium storage, Chem. Eng. J. 450 (2022), 138453.

[10] G. Li, X. Lou, C. Peng, C. Liu, W. Chen, Interface chemistry for sodium metal anodes/batteries: a review, Chem. Synth. 2 (2022) 16.

[11] Y. Xu, K. Wang, J. Han, C. Liu, Y. An, Q. Meng, C. Li, X. Zhang, X. Sun, Y. Zhang, L. Mao, Z. Wei, Y. Ma, Scalable production of wearable solid-state Li-ion capacitors from N-doped hierarchical carbon, Adv. Mater. 32 (45) (2020) 2005531.

[12] T. Liang, Z. Mao, L. Li, R. Wang, B. He, Y. Gong, J. Jin, C. Yan, H. Wang, A mechanically flexible necklace-like architecture for achieving fast charging and high capacity in advanced lithium-ion capacitors, Small 18 (27) (2022) 2201792.

[13] W. Liu, X. Zhang, Y. Xu, C. Li, K. Wang, X. Sun, F. Su, C.-M. Chen, F. Liu, Z.-S. Wu, Y. Ma, Recent advances on carbon-based materials for high performance lithium-ion capacitors, Batteries Supercaps 4 (3) (2021) 407–428.

[14] L.-N. Hu, X.-Z. Li, Z.-C. Lv, Y.-R. Zhu, J.-H. Zhang, T.-F. Yi, Design of Sb_2Se_3-based nanocomposites for high-performance alkali metal ion batteries driven by a hybrid charge storage mechanis, Chem. Eng. J. 440 (2022), 135971.

[15] C. Choi, D.S. Ashby, D.M. Butts, R.H. DeBlock, Q. Wei, J. Lau, B. Dunn, Achieving high energy density and high power density with pseudocapacitive materials, Nat. Rev. Mater. 5 (2020) 5–19.

[16] L. Qin, Y. Liu, S. Xu, S. Wang, X. Sun, S. Zhu, L. Hou, C. Yuan, In-plane assembled single-crystalline T-Nb_2O_5 nanorods derived from few-layered Nb_2CT_x MXene nanosheets for advanced Li-ion capacitors, Small Methods 4 (12) (2020) 2000630.

[17] Y. Zheng, W. Qiu, L. Wang, J. Liu, S. Chen, C. Li, Triple conductive wiring by electron doping, chelation coating and electrochemical conversion in fluffy Nb_2O_5 anodes for fast-charging Li-ion batteries, Adv. Sci. 9 (25) (2022) 2202201.

[18] P. Jing, K. Liu, L. Soule, J. Wang, T. Li, B. Zhao, M. Liu, Engineering the architecture and oxygen deficiency of T-Nb_2O_5-carbon-graphene composite for high-rate lithium-ion batteries, Nano Energy 89 (2021), 106398.

[19] J. Chen, J. Meng, K. Han, F. Liu, W. Wang, Q. An, L. Mai, Crystal structure regulation boosts the conductivity and redox chemistry of T-Nb_2O_5 anode material, Nano Energy 110 (2023), 108377.

[20] P. Barnes, Y. Zuo, K. Dixon, D. Hou, S. Lee, Z. Ma, J.G. Connell, H. Zhou, C. Deng, K. Smith, E. Gabriel, Y. Liu, O.O. Maryon, P.H. Davis, H. Zhu, Y. Du, J.i. Qi, Z. Zhu, C. Chen, Z. Zhu, Y. Zhou, P.J. Simmonds, A.E. Briggs, D. Schwartz, S.P. Ong, H. Xiong, Electrochemically induced amorphous-to-rock-salt phase transformation in niobium oxide electrode for Li-ion batteries, Nat. Mater. 21 (7) (2022) 795–803.

[21] M. Yang, S. Li, J. Huang, Three-dimensional cross-linked Nb_2O_5 polymorphs derived from cellulose substances: insights into the mechanisms of lithium storage, ACS Appl. Mater. Interfaces 13 (33) (2021) 39501–39512.

[22] J. Meng, Q. He, L. Xu, X. Zhang, F. Liu, X. Wang, Q. Li, X. Xu, G. Zhang, C. Niu, Z. Xiao, Z. Liu, Z. Zhu, Y. Zhao, L. Mai, Identification of phase control of carbon-confined Nb_2O_5 nanoparticles toward high-performance lithium storage, Adv. Energy Mater. 9 (18) (2019) 1802695.

[23] Q. Ji, Z. Xu, X. Gao, Y.-J. Cheng, X. Wan, X. Zuo, G.Z. Chen, B. Hu, J. Zhu, P. G. Bruce, Y. Xia, Carbon-emcoating architecture boosts lithium storage of Nb_2O_5, Sci. China Mater. 64 (5) (2021) 1071–1086.

[24] Y. Zheng, Z. Yao, Z. Shadike, M. Lei, J. Liu, C. Li, Defect-concentration-mediated T-Nb_2O_5 anodes for durable and fast-charging Li-ion batteries, Adv. Funct. Mater. 32 (12) (2022) 2107060.

[25] Y. Zhang, L. Tao, C. Xie, D. Wang, Y. Zou, R. Chen, Y. Wang, C. Jia, S. Wang, Defect engineering on electrode materials for rechargeable batteries, Adv. Mater. 32 (7) (2020) 1905923.

[26] P. Xiong, X. Zhang, F. Zhang, D. Yi, J. Zhang, B. Sun, H. Tian, D. Shanmukaraj, T. Rojo, M. Armand, R. Ma, T. Sasaki, G. Wang, Two-dimensional unilamellar cation-deficient metal oxide nanosheet superlattices for high-rate sodium ion energy storage, ACS Nano 12 (12) (2018) 12337–12346.

[27] H. Zhu, Q. Wei, S. Yu, P. Guo, J. Li, Y. Wang, Synthesis of hollow nanostructures based on iron oxides and their applications in lithium-ion batteries, J. Electron. Mater. 51 (8) (2022) 4207–4223.

[28] Y. Liu, C. Xiao, Z. Li, Y. Xie, Vacancy engineering for tuning electron and phonon structures of two-dimensional materials, Adv. Energy Mater. 6 (23) (2016) 1600436.

[29] Y. Zhang, P. Chen, Q. Wang, Q. Wang, K. Zhu, K. Ye, G. Wang, D. Cao, J. Yan, Q. Zhang, High-capacity and kinetically accelerated lithium storage in MoO_3 enabled by oxygen vacancies and heterostructure, Adv. Energy Mater. 11 (31) (2021) 2101712.

[30] S. Fleischmann, J.B. Mitchell, R. Wang, C. Zhan, D.E. Jiang, V. Presser, V. Augustyn, Pseudocapacitance: from fundamental understanding to high power energy storage materials, Chem. Rev. 120 (14) (2020) 6738–6782.

[31] X. Xiao, X. Deng, Y. Tian, S. Tao, Z. Song, W. Deng, H. Hou, G. Zou, X. Ji, Ultrathin two-dimensional nanosheet metal-organic frameworks with high-density ligand active sites for advanced lithium-ion capacitors, Nano Energy 103 (2022), 107797.

[32] L. Yao, Q. Gu, X. Yu, Three-dimensional MOFs@MXene aerogel composite derived MXene threaded hollow carbon confined CoS nanoparticles toward advanced akali-ion batteries, ACS Nano 15 (2) (2021) 3228–3240.

[33] B. Yang, B. Liu, J. Chen, Y. Ding, Y. Sun, Y. Tang, X. Yan, Realizing high-performance lithium ion hybrid capacitor with a 3D MXene-carbon nanotube composite anode, Chem. Eng. J. 429 (2022), 132392.

[34] Y.-L. Wang, L.-Q. Fan, S.-J. Sun, J.-J. Chen, Z.-X. Wu, T.-T. Zhu, Y.-F. Huang, J.-H. Wu, $Ti_3C_2T_x$ MXene supported SnO_2 quantum dots with oxygen vacancies as anode for Li-ion capacitors, Chem. Eng. J. 428 (2022), 131993.

[35] W. Zhong, M. Tiao, W. Tang, W. Gao, T. Yang, Y. Zhang, R. Zhan, S.-J. Bao, M. Xu, MXene-derivative pompon-like $Na_2Ti_3O_7$@C anode material for advanced sodium ion batteries, Chem. Eng. J. 378 (2019), 122209.

[36] L. Qin, Y. Liu, S. Zhu, D. Wu, G. Wang, J. Zhang, Y. Wang, L. Hou, C. Yuan, Formation and operating mechanisms of single-crystalline perovskite $NaNbO_3$ nanocubes few-layered Nb_2CT_x MXene hybrids towards Li-ion capacitors, J. Mater. Chem. A 9 (36) (2021) 20405–20416.

[37] L. Wang, X. Zhang, Y. Xu, C. Li, W. Liu, S. Yi, K. Wang, X. Sun, Z.S. Wu, Y. Ma, Tetrabutylammonium-intercalated 1T-MoS_2 nanosheets with expanded interlayer spacing vertically coupled on 2D delaminated MXene for high-performance lithium-ion capacitors, Adv. Funct. Mater. 31 (36) (2021) 2104286.

[38] X. Zhang, L. Wang, W. Liu, C. Li, K. Wang, Y. Ma, Recent advances in MXenes for lithium-ion capacitors, ACS Omega 5 (1) (2020) 75–82.

[39] C. Li, X. Zhang, K. Wang, X. Sun, Y. Ma, Accordion-like titanium carbide (MXene) with high crystallinity as fast intercalative anode for high-rate lithium-ion capacitors, Chin. Chem. Lett. 31 (4) (2020) 1009–1013.

[40] Z.-M. Qiu, Y. Bai, Y.-D. Gao, C.-L. Liu, Y. Ru, Y.-C. Pi, Y.-Z. Zhang, Y.-S. Luo, H. Pang, MXenes nanocomposites for energy storage and conversion, Rare Met. 41 (4) (2022) 1101–1128.

[41] F. Li, Y.-L. Liu, G.-G. Wang, S.-Y. Zhang, D.-Q. Zhao, K. Fang, H.-Y. Zhang, H. Y. Yang, 3D porous H-$Ti_3C_2T_x$ films as free-standing electrodes for zinc ion hybrid capacitors, Chem. Eng. J. 435 (2022), 135052.

[42] V. Natu, M. Sokol, L. Verger, M.W. Barsoum, Effect of edge charges on stability and aggregation of $Ti_3C_2T_z$ MXene colloidal suspensions, J. Phys. Chem. C 122 (48) (2018) 27745–27753.

[43] V. Natu, J.L. Hart, M. Sokol, H. Chiang, M.L. Taheri, M.W. Barsoum, Edge capping of 2D-MXene sheets with polyanionic salts to mitigate oxidation in aqueous colloidal suspensions, Angew. Chem. Int. Ed. 58 (36) (2019) 12655–12660.

[44] Z.-L. Tan, J.-X. Wei, Y. Liu, F. Zaman, W. Rehman, L.-R. Hou, C.-Z. Yuan, V_2CT_x MXene and its derivatives: synthesis and recent progress in electrochemical energy storage applications, Rare Met. 41 (3) (2022) 775–797.

[45] Y. Wang, M. Qiao, Y. Li, S. Wang, Tuning surface electronic configuration of NiFe LDHs nanosheets by introducing cation vacancies (Fe or Ni) as highly efficient electrocatalysts for oxygen evolution reaction, Small 14 (17) (2018) 1800136.

[46] Y. Liu, H. Cheng, M. Lyu, S. Fan, Q. Liu, W. Zhang, Y. Zhi, C. Wang, C. Xiao, S. Wei, B. Ye, Y. Xie, Low overpotential in cacancy-rich ultrathin $CoSe_2$ nanosheets for water oxidation, J. Am. Chem. Soc. 136 (44) (2014) 15670–15675.

[47] M. Naguib, J. Halim, J. Lu, K.M. Cook, L. Hultman, Y. Gogotsi, M.W. Barsoum, New two-dimensional niobium and vanadium carbides as promising materials for Li-ion batteries, J. Am. Chem. Soc. 135 (43) (2013) 15966–15969.

[48] J. Zhao, J. Wen, J. Xiao, X. Ma, J. Gao, L. Bai, H. Gao, X. Zhang, Z. Zhang, Nb_2CT_x MXene: high capacity and ultra-long cycle capability for lithium-ion battery by regulation of functional groups, J. Energy Chem. 53 (2021) 387–395.

[49] K. Guan, L. Dong, Y. Xing, X. Li, J. Luo, Q. Jia, H. Zhang, S. Zhang, W. Lei, Structure and surface modification of MXene for efficient Li/K-ion storage, J. Energy Chem. 75 (2022) 330–339.

[50] S. Hemmati, G. Li, X. Wang, Y. Ding, Y. Pei, A. Yu, Z. Chen, 3D N-doped hybrid architectures assembled from 0D T-Nb_2O_5 embedded in carbon microtubes toward high-rate Li-ion capacitors, Nano Energy 56 (2019) 118–126.

[51] W. Zhao, W. Zhao, G. Zhu, T. Lin, F. Xu, F. Huang, Black Nb_2O_5 nanorods with improved solar absorption and enhanced photocatalytic activity, Dalton Trans. 45 (9) (2016) 3888–3894.

[52] H. Takemura, M. Kotoku, M. Yasutake, T. Shinmyozu, 9-fluoro-18-hydroxy-[3.3] metacyclophane: synthesis and estimation of a C-F···H-O hydrogen bond, Eur. J. Org. Chem. 2004 (9) (2004) 2019–2024.

[53] T. Hiroyuki, K. Hiroyuki, Y. Mikio, K. Noriyoshi, T. Keita, S. Katsuya, S. Teruo, I. Takahiko, Syntheses of macrocyclic compounds possessing fluorine atoms in their cavities: structures and complexation with cations, Eur. J. Org. Chem. 2000 (1) (2000) 141–148.

[54] K.G. Myakishev, E.A. Il'inchik, V.V. Volkov, Synthesis and properties of isopropylamine borane i–$C_3H_7NH_2{\cdot}BH_3$, Russ. J. Inorg. Chem. 57 (9) (2012) 1291–1294.

[55] Z. Gao, S. Zeng, B. Zhu, B. Li, Q. Hao, Y. Hu, D. Wang, K. Tang, A FeSe-based superconductor $(C_2H_8N_2)_x$ FeSe with only ethylenediamine intercalated, Sci. China Mater. 61 (7) (2018) 977–984.

[56] Z.-X. Deng, C. Wang, X.-M. Sun, Y.-D. Li, Structure-directing coordination template effect of ethylenediamine in formations of ZnS and ZnSe nanocrystallites via solvothermal route, Inorg. Chem. 41 (4) (2002) 869–873.

[57] S. Doo, A. Chae, D. Kim, T. Oh, T.Y. Ko, S.J. Kim, D.Y. Koh, C.M. Koo, Mechanism and kinetics of oxidation reaction of aqueous $Ti_3C_2T_x$ suspensions at different pHs and temperatures, ACS Appl. Mater. Interfaces 13 (19) (2021) 22855–22865.

[58] J. Xiong, L. Wen, F. Jiang, Y. Liu, S. Liang, L. Wu, Ultrathin HNb_3O_8 nanosheet: an efficient photocatalyst for the hydrogen production, J. Mater. Chem. A 3 (41) (2015) 20627–20632.

[59] W. Grünert, R. Feldhaus, K. Anders, E.S. Shpiro, G.V. Antoshin, K.M. Minachev, A new facility for inert transfer of reactive samples to XPS equipment, J. Electron. Spectrosc. Relat. Phenom. 40 (2) (1986) 187–192.

[60] S. Badrinarayanan, S. Sinha, X-ray photoelectron spectroscopy studies of the reaction of N_2^+-ion beams with niobium and tantalum metals, J. Appl. Phys. 69 (1991) 1141.

[61] D. Li, J. Shi, H. Liu, C. Liu, G. Dong, H. Zhang, Y. Yang, G. Lu, H. Wang, T-Nb_2O_5 embedded carbon nanosheet with superior reversibility and rate capability as an anode for high energy Li-ion capacitors, Sustain. Energy Fuels 3 (4) (2019) 1055–1065.

[62] J. Miao, Q. Zhu, K. Li, P. Zhang, Q. Zhao, B. Xu, Self-propagating fabrication of 3D porous MXene-rGO film electrode for high-performance supercapacitors, J. Energy Chem. 52 (2021) 243–250.

[63] Y. An, T. Liu, C. Li, X. Zhang, T. Hu, X. Sun, K. Wang, C. Wang, Y. Ma, A general route for the mass production of graphene-enhanced carbon composites toward practical pouch lithium-ion capacitors, J. Mater. Chem. A 9 (28) (2021) 15654–15664.

[64] Z. Song, H. Li, W. Liu, H. Zhang, J. Yan, Y. Tang, J. Huang, H. Zhang, X. Li, Ultrafast and stable Li-(de)intercalation in a large single crystal H-Nb_2O_5 anode via optimizing the homogeneity of electron and ion transport, Adv. Mater. 32 (22) (2020) 2001001.

[65] H. Kim, E. Lim, C. Jo, G. Yoon, J. Hwang, S. Jeong, J. Lee, K. Kang, Ordered-mesoporous Nb_2O_5/carbon composite as a sodium insertion material, Nano Energy 16 (2015) 62–70.

[66] W. Liu, X. Zhang, Y. Xu, L. Wang, Z. Li, C. Li, K. Wang, X. Sun, Y. An, Z.-S. Wu, Y. Ma, 2D graphene/MnO heterostructure with strongly stable interface enabling high-performance flexible solid-state lithium-ion capacitors, Adv. Funct. Mater. 32 (30) (2022) 2202342.

[67] S. Yi, L. Wang, X. Zhang, C. Li, W. Liu, K. Wang, X. Sun, Y. Xu, Z. Yang, Y. Cao, J. Sun, Y. Ma, Cationic intermediates assisted self-assembly two-dimensional $Ti_3C_2T_x$/rGO hybrid nanoflakes for advanced lithium-ion capacitors, Sci. Bull. 66 (9) (2021) 914–924.

[68] E. Lim, C. Jo, H. Kim, M.-H. Kim, Y. Mun, J. Chun, Y. Ye, J. Hwang, K.-S. Ha, K.C. Roh, K. Kang, S. Yoon, J. Lee, Facile synthesis of Nb_2O_5 @carbon core-shell nanocrystals with controlled crystalline structure for high-power anodes in hybrid supercapacitors, ACS Nano 9 (7) (2015) 7497-7505.

[69] M.Y. Song, N.R. Kim, H.J. Yoon, S.Y. Cho, H.J. Jin, Y.S. Yun, Long-lasting Nb_2O_5-based nanocomposite materials for Li-ion storage, ACS Appl. Mater. Interfaces 9 (3) (2017) 2267–2274.

[70] C.H. Lai, D. Ashby, M. Moz, Y. Gogotsi, L. Pilon, B. Dunn, Designing pseudocapacitance for Nb_2O_5/carbide-derived carbon electrodes and hybrid devices, Langmuir 33 (37) (2017) 9407–9415.

[71] J. Wang, H. Li, L. Shen, S. Dong, X. Zhang, Nb_2O_5 nanoparticles encapsulated in ordered mesoporous carbon matrix as advanced anode materials for Li ion capacitors, RSC Adv. 6 (75) (2016) 71338–71344.